Understanding air–water mass transfer in rectangular dropshafts[1]

H. Chanson

Abstract: A dropshaft is a vertical structure connecting two channels with different invert elevations. Four configurations of rectangular dropshafts were investigated systematically to study the effects of outflow direction and pool depth on particle residence times and flow aeration. The best hydraulic design was that with 180° outflow direction and deep pool shaft. For that design, a full-scale study was conducted, the scaling ratio between prototype and model being 3.1:1. Although similar trends were seen in both model and prototype, scale effects were observed in terms of particle residence times and bubble swarm depths. In the prototype, detailed air–water flow measurements were performed in the shaft pool and the mass transfer equation was integrated using measured interfacial areas and particle residence times. The results demonstrate that the air–water mass transfer is the largest at low flow rates (regime R1) because of large residence times and significant interfacial area. Overall the present study provides new understanding of the basic mechanisms of air–water mass transfer in rectangular dropshafts.

Key words: dropshaft, mass transfer, aeration, hydraulics.

Résumé : Un puits de rupture est une structure verticale réunissant deux canalisations à différentes élévations du bas. Quatre configurations de puits de rupture rectangulaires ont été examinées systématiquement afin d'étudier les effets de la direction de l'exutoire et la profondeur du bassin sur les temps de rétention des particules et l'aération de l'écoulement. La meilleure conception hydraulique consistait en une direction de l'exutoire de 180° et un puits avec un bassin profond. Pour cette conception, une étude à grande échelle a été effectuée avec un rapport de mise à l'échelle de 3,1:1 entre le prototype et le modèle. Bien que des tendances similaires aient été constatées à la fois dans le modèle et le prototype, les effets d'échelle ont été observés en termes de temps de rétention des particules et de profondeur des essaims de bulles. Dans le prototype, des mesures détaillées de l'écoulement air-eau ont été prélevées dans le bassin du puits et l'équation de transfert de masse a été intégrée en utilisant les zones interfaciales mesurées et les temps de rétention des particules. Les résultats démontrent que le transfert de masse air-eau est supérieur à des taux d'écoulement faibles (régime R1) en raison des temps de rétention prolongés et d'une zone interfaciale importante. Règle générale, la présente étude fournit une nouvelle compréhension des mécanismes de base du transfert de masse air-eau dans les puits de rupture rectangulaires.

Mots clés : puits de rupture, transfert de masse, aération, hydraulique.

[Traduit par la Rédaction]

Introduction

A dropshaft is a vertical structure connecting two channels with different invert elevations (Figs. 1 and 2). Figure 1 presents a full-scale dropshaft (Prototype AA) operating under controlled flow conditions in laboratory. Figure 1a shows a small discharge while Fig. 1b illustrates a large flow rate. Dropshafts are commonly used in sewers and storm water systems: e.g., in Münich, Paris, Tokyo (Rajaratnam et al. 1997; Toda and Inoue 1999; Merlein et al. 2002). Small dropshafts are also used upstream and downstream of culverts (Apelt 1984), while large spillway

shafts were built (Vischer and Hager 1998). The dropshaft is an ancient design. For example, some Roman aqueducts included series of dropshafts (Chanson 2002a). There is however a controversy if these dropshafts were used solely for energy dissipation or in combination with flow re-aeration, but it will be shown that their design was efficient for both applications. Despite such long usage, the hydraulics of dropshafts has not been systematically documented, but for a few studies: Apelt (1984); Rajaratnam et al. (1997); Merlein et al. (2002).

In modern water treatment plants, the combination of flow aeration and high flow turbulence greatly enhances the mass transfer of volatile organic compunds such as chlorine (Corsi et al. 1992). Detailed studies of mass transfer at dropshafts are limited however (Rahme et al. 1997). The literature often relies upon air–water mass transfer experimental results at free-overfall and drop structures: e.g., Avery and Novak (1978); Nakasone (1987).

Basic equations of air–water gas transfer

Fick's law states that the mass transfer rate of a chemical across an interface normal to the x-direction and in a quiescent

Fig. 1. Rectangular dropshaft in operation (shaft dimensions: 0.76 m × 0.75 m). (*a*) Regime R1 — Flow from the top right to the bottom left. Note the bubbly flow region of the free-jet impact into the shaft pool. (*b*) Regime R3 — Flow from the top right to the bottom left. Note the jet impact onto the opposite wall, the "white waters" in the shaft pool, and the highly-aerated outflow channel waters.

(a)

(b)
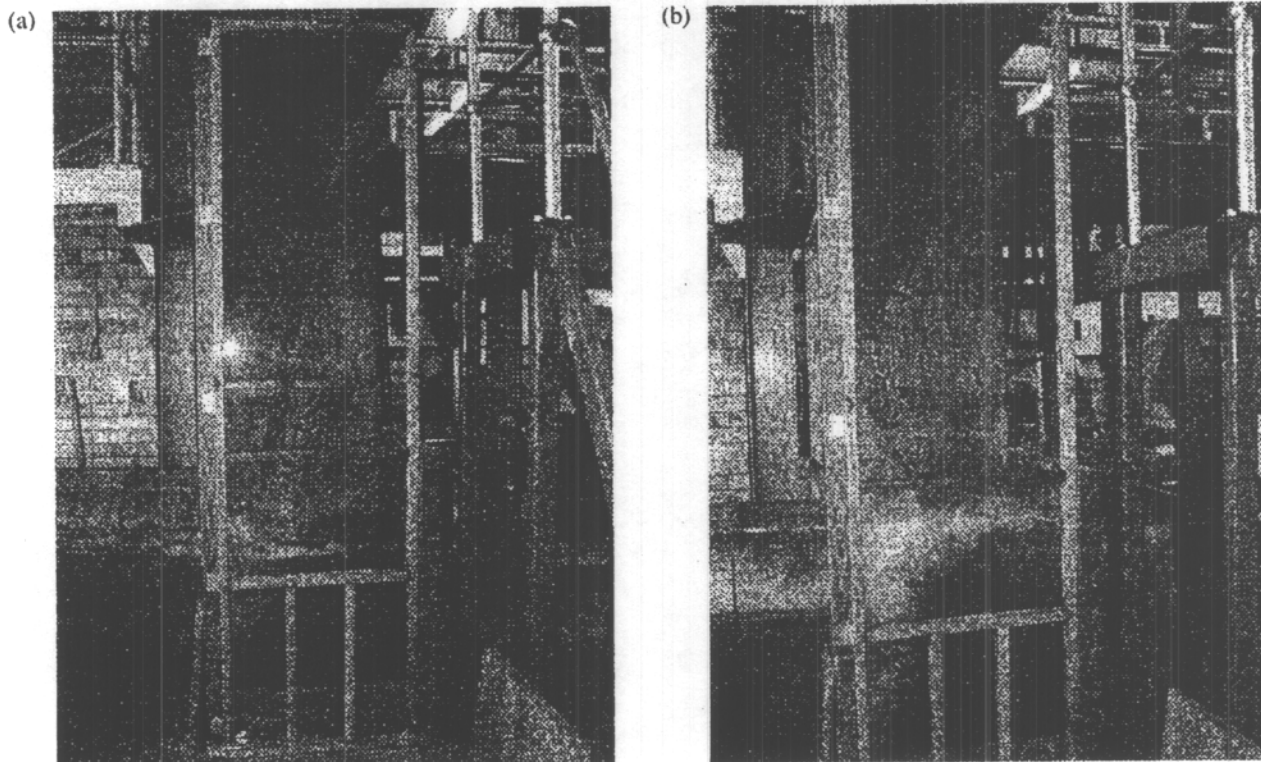
fluid varies directly as the coefficient of molecular diffusion D_{gas} and the negative gradient of gas concentration

$$[1] \qquad \frac{\partial}{\partial t} M_{gas} \propto -D_{gas} \left(\frac{\partial}{\partial x} C_{gas} \right)$$

where C_{gas} is the concentration of the dissolved chemical in liquid and t is the time. The analysis of the fluid layers surrounding a gas bubble is very complicated because of the bubble shape, the presence of laminar or turbulent flow, a mobile interface in the case of large air bubbles and the interactions between concentration boundary layers from adjacent bubbles. When the particular chemical is volatile (e.g., oxygen, chlorine), the transfer is controlled by the liquid phase and the coefficient of transfer is almost equal to the liquid film coefficient, which is a function of the salinity, temperature, surfactants, and to a lesser extent the pressure. For volatile gas in a liquid, the mass transfer eq. [1] becomes

$$[2] \qquad \frac{\partial}{\partial t} C_{gas} = K_L a \left(C_s - C_{gas} \right)$$

where a is the specific surface area defined as the air–water interface area per unit volume of air and water, C_s is the concentration of dissolved gas in water at equilibrium, and K_L is the liquid film coefficient (Gulliver 1990, Jirka 1991). Although some studies implied that the term $(K_L a)$ was constant, this assumption is incorrect. Detailed studies showed that the

mass transfer coefficient K_L in turbulent gas–liquid flows is almost constant regardless of bubble sizes and flow situations (Kawase and Moo-Young 1992), but the interface area varies greatly along a hydraulic structure as a function of the air–water flow properties.

Equation [2] demonstrates that the rate of mass transfer is proportional to the residence time and air–water interfacial area. In a dropshaft, both contributions are significant (see below) and the mass transfer of chemicals is significant. The large amount of entrained air bubbles increases the air–water interface area due to the cumulative bubble surface area. For oxygen transfer at drop structures, Corsi et al. (1992) observed a linear increase of the coefficient of transfer ($K_L A$) with increasing drop heights or discharges when the other parameter was held constant, where A is the total air–water interface area. Their experiments also showed that the volatile organic compound (VOC) emission of a 2 m high drop structure was significant.

It is the purpose of this paper to detail the hydraulics and aeration properties of rectangular dropshaft designs. Detailed experiments were conducted systematically in four configurations (Table 1) with a focus on residence time and flow aeration. For the most efficient design, new air–water flow measurements were performed in a full-scale structure. The results provide an unique understanding of air–water mass transfer characteristics in rectangular dropshafts.

Fig. 2. Definition sketch — Flow from top left to bottom right. (*a*) Shaft with 180* outflow direction and regime R1. (*b*) Shaft with 90° outflow direction and regime R3.
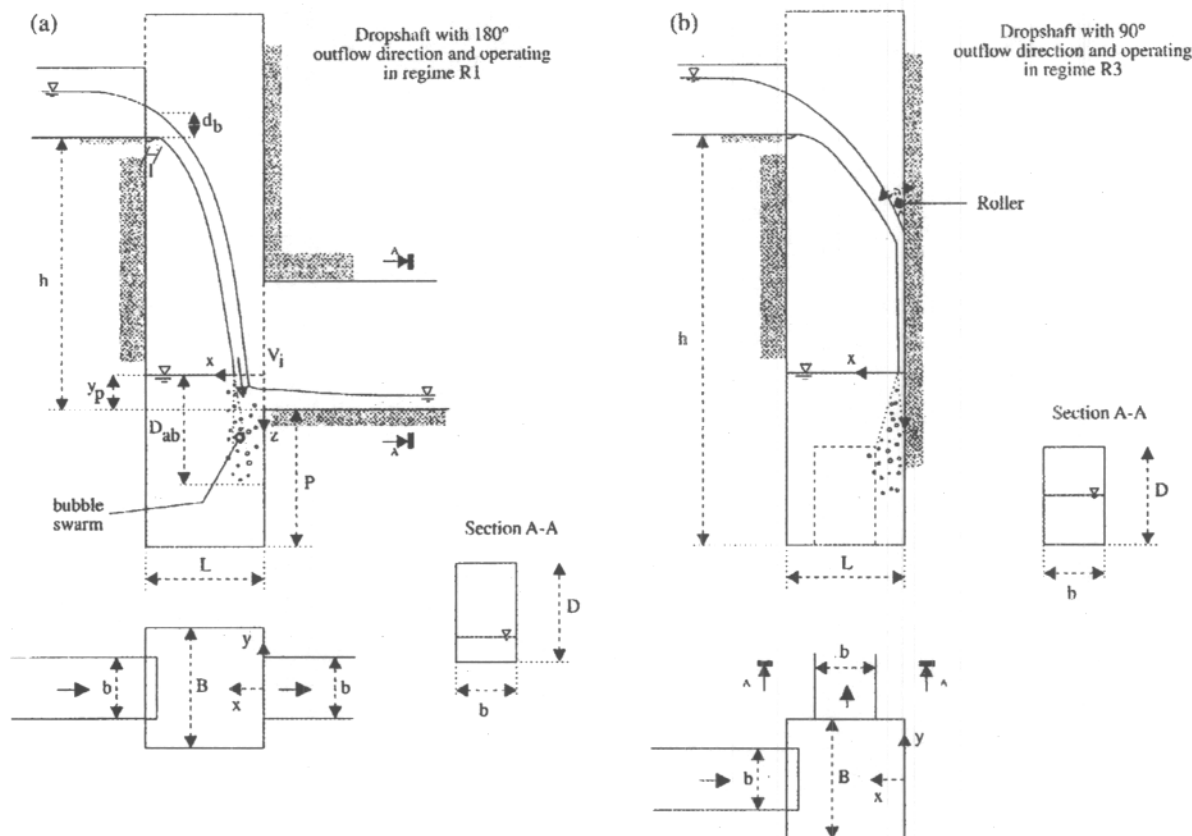

Table 1. Experimental investigations of rectangular dropshafts.

Reference	h (m)	P (m)	L (m)	B (m)	l (m)	b_1 (m)	$D_1{}^a$(m)	b_2 (m)	D_2 (m)	Outflow direction (°)
Present study										
Prototype AA	1.7	1	0.755	0.763	0.12	0.5	0.3	0.5	0.3	180
Model A	0.548	0.322	0.243	0.246	0.04	0.161	0.25	0.209	0.1	180
Model B	0.548	0.322	0.243	0.246	0.04	0.161	0.25	0.209	0.1	90
Model C	0.548	0	0.243	0.246	0.04	0.161	0.25	0.209	0.1	180
Model D	0.548	0	0.243	0.246	0.04	0.161	0.25	0.209	0.1	90
Chanson (2002*a*)										
Recret model	0.505	0.365	0.3	0.3	0	0.144	0.25	0.15	0.25	180
Valdepuentes model 1	0.668	0.201	0.2	0.3	0	0.11	0.25	0.11	0.21	90
Valdepuentes model 2	0.668	0.201	0.2	0.3	0	0.11	0.25	0.11	0.21	180
Apelt (1984)	0.325	0	0.152	0.152	0	Pipe: $\emptyset = 0.152$ m		Pipe: $\emptyset = 0.152$ m		180

Note: For notation see Fig. 2.
^{a}Sidewall height.

Experimental setup

Four dropshaft geometries were studied basically in two flumes (Table 1, Fig. 1). Four models were built in marine plywood and perspex with a vertical rectangular shaft. The upstream channels were open while the downstream conduits were covered and ended with a free overfall. Both upstream and downstream channels were horizontal. All the shaft dimensions were identical, but for the outflow direction (i.e., 90° and 180°) and the presence (or absence) of deep shaft pool (Fig. 2). A full-scale shaft was built (Prototype AA) corresponding to Model A

configuration (Fig. 1, Table 1). The prototype was designed to be geometrically similar based upon a Froude similitude with undistorted scale (e.g., Henderson 1966; Chanson 1999, 2004). The geometric scaling ratio was $L_R = 3.1$. Similar experiments were conducted for identical dimensionless inflow critical depth d_c / h where d_c is the critical depth at the brink and h is the invert drop in elevation.

Instrumentation

In laboratory models, the discharges were deduced from the brink depth measurements that were first calibrated in situ with volume-per-time discharge data. In the full-scale shaft, the flows rates were estimated from bend meters that were calibrated in situ with a 90° V-notch weir.

Free-surface elevations were recorded with pointer gauges in the upstream and downstream channels, while the free-surface height in the shaft was measured with rulers. The total head was measured with a total head tube ($\emptyset = 1$ mm). Measurements were conducted at five transverse profiles and averaged over the cross section. The averaging method was particularly important in the 90° bend dropshaft configurations and in the prototype shaft.

Particle residence times were recorded using neutrally-buoyant particles (relative density between 0.95 and 1.05) made of wax and aluminium. Several particle sizes were used: 3.3, 3.9, 5, 9, and 15 mm. The four smallest sizes were used in the models while the three largest sizes were used in the prototype. The particles were introduced, one at a time, in the inflow channel about 1 m upstream of the brink and each particle was collected at the downstream end of the outflow channel, before the next particle was injected. The total travel times were recorded with digital chronometers. The residence time in the shaft was determined by subtracting the calculated travel times in the inflow and outflow channels to the measured time.

Air–water flow properties were measured with a single-tip conductivity probe (needle probe design). The probe consisted of a sharpened rod (platinum wire $\emptyset = 0.35$ mm) that was insulated except for its tip and set into a metal supporting tube (stainless steel surgical needle $\emptyset = 1.42$ mm) acting as the second electrode. The probe was excited by an air bubble detector (Ref. AS25240) designed with a response time less than 10 μs and calibrated with a square wave generator. During the present study, the probe output signal was scanned at 5 kHz for 3 min.

Additional information were obtained with high-speed photography and video camera. Further details and all the data set were reported in Chanson (2002b).

Data processing

The measurement principle of conductivity probes is based upon the difference in electrical resistivity between air and water. The air concentration, or void fraction C, is the proportion of time that the probe tip is in the air. Past experience showed that the probe orientation with the flow direction has little effect on the void fraction accuracy provided that the probe support does not affect the flow past the tip (e.g., Sene 1984). In the

Fig. 3. Comparison between measured specific interface area for eqs. [3] and [4] for the plunging jet data of Cummings and Chanson (1997): vertical supported jet, $d_i = 0.012$ m, $V_i = 6.0$ m/s. (Data from Cummings and Chanson, $V_i = 6.0$ m/s, $z = 0.005$ to 0.25 m.)
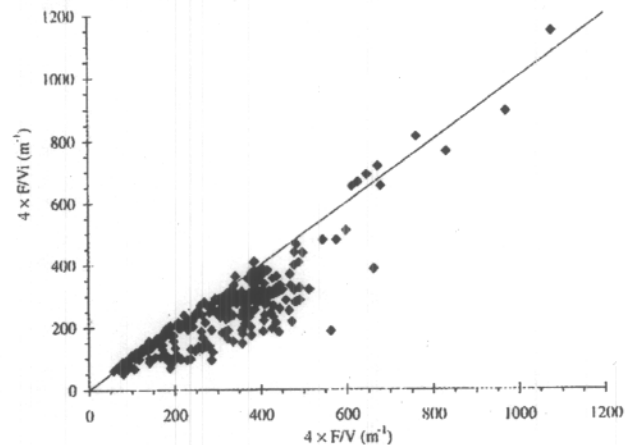
present study, the probe tip was aligned with the flow direction. The bubble count rate F is the number of bubbles impacting the probe tip. The measurement is sensitive to the probe tip size, bubble sizes, velocity, and discrimination technique, particularly when the sensor size is larger than the smallest bubble sizes.

For any bubble size distribution and chord length distribution, the specific air–water interface area derives from the mass conservation for air

$$[3] \qquad a = \frac{4F}{V}$$

where V is the local velocity. The derivation of eq. [3] is simple for spherical particles. It may be extended to ellipsoidal particles following the method of Clark and Turton (1988) (also Moursali et al. 1995). In the present study, the velocity was not measured and the specific interface area was approximated as

$$[4] \qquad a \approx \frac{4F}{V_i}$$

where V_i is the free-falling nappe impact velocity deduced from basic trajectory equations (Fig. 2). For plunging jet flow data of Cummings and Chanson (1997), a comparison between eq. [3] and eq. [4] shows that eq. [4] underestimates the measured specific interface area of that determined by eq. [3] by 20% on average (Fig. 3).

Hydraulic properties

Basic flow patterns

The upstream and downstream channels operated as free-surface flow for all investigated flow conditions. The inflow conditions were subcritical, while the outflow channel operated

Table 2. Flow conditions d_c/h for the change in flow regimes.

	180° outflow direction			90° outflow direction		
Configuration	R1–R2	R2–R3a	R3a–R3b	R1–R3a	R3a–R3b	Remarks
Prototype AA	0.037	0.046	—	n/a	n/a	$P = 1.0$ m
Model A	0.039	0.051	0.1	n/a	n/a	$P = 0.32$ m
Model C	0.038	0.046	0.099	n/a	n/a	$P = 0$
Model B	n/a	n/a	n/a	0.037	0.12	$P = 0.32$ m
Model D	n/a	n/a	n/a	0.035	0.11	$P = 0$
Recret model	0.09	0.175	—	n/a	n/a	$P = 0.36$ m
Valdepuentes model 2	0.029	0.042	—	n/a	n/a	$P = 0.20$ m
Valdepuentes model 1	n/a	n/a	n/a	0.028	—	$P = 0.20$ m

Note: —, information not available.

Fig. 4. Dimensionless residual head H_{res}/H_1 as a function of the dimensionless flow rate d_c/h.
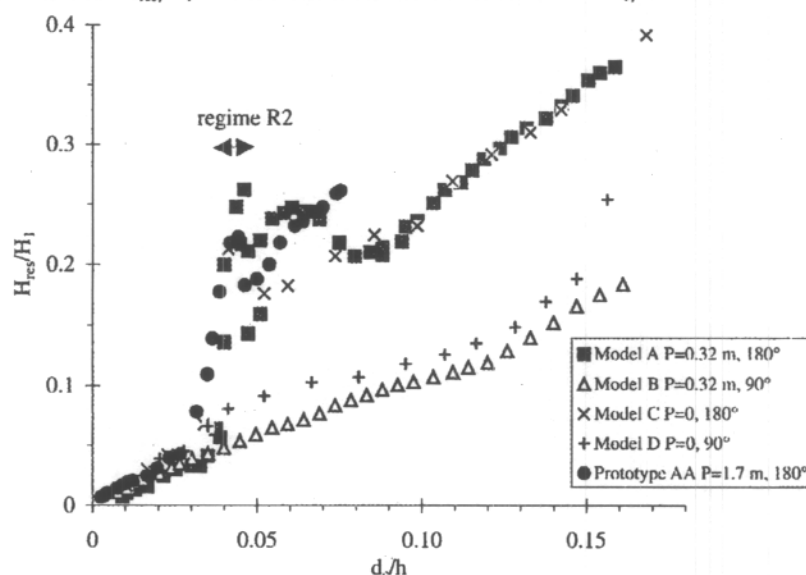
with supercritical flows. Chanson (2002a) and Rajaratnam et al. (1997) reported a similar finding.

Three flow regimes were observed as functions of the flow rate for 180° shaft configurations (Table 2). At low flow rates, the free-falling nappe impacted into the shaft pool (regime R1, Figs. 1a and 2a). Substantial air bubble entrainment took place in the shaft pool. In the downstream channel, the flow was supercritical and shock waves developed. For intermediate discharges, the free-falling nappe impacted into the outflow channel (regime R2). The pool free-surface level increased significantly, almost no air bubble entrainment was seen in the pool and very intense invert pressures were observed in the outflow channel. At large flow rates, the free-jet impacted onto the opposite wall above the downstream conduit obvert (regime R3) (Fig. 1b). Significant water deflections took place in the shaft associated with substantial air entrainment in the shaft pool. For the largest flow rates, the outflow channel inlet became submerged (regime R3b). These observations were consistent with

the earlier study of Chanson (2002a), although the downstream conduit was higher and the sub-regime R3b was not observed then.

For a 90° shaft configuration, the above observations were generally valid, but the regime R2 did not exist (Table 2). Only regimes R1, R3a (free-surface outflow channel inlet), and R3b (submerged outflow channel inlet) were observed. In the models with no pool (i.e., $P = 0$), the same findings were basically valid, but air entrainment in the shaft was limited by the shallow invert while greater splashing was seen in the shaft.

Energy dissipation

Residual energy data are presented in Fig. 4. The data are presented as H_{res}/H_1 as a function of the dimensionless flow rate d_c/h where H_{res} is the specific energy in the downstream channel, H_1 is the upstream total head measured above the downstream channel invert, d_c is the critical depth in the upstream channel, and h is the drop in invert elevation. The results showed

Fig. 5. Dimensionless bubble penetration depth $D_{ab}/(y_p + h)$ as a function of the dimensionless flow rate d_c/h (dropshafts with deep pool).
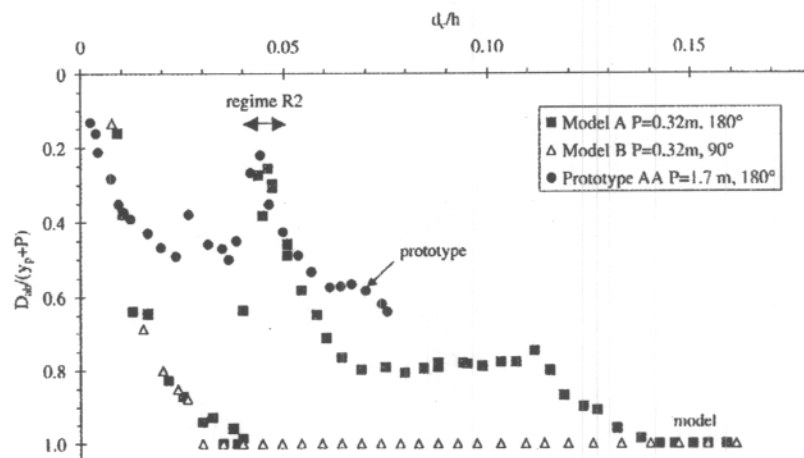
small residual heads, associated with high energy dissipation, at low flow rates (regime R1) (Fig. 4). Poor dissipation performances are observed in regime R2. In regime R3, the dimensionless residual head ranges from 20 to 35% depending upon the model geometry. Note the relatively good agreement between model and prototype data. Comparative results showed that the absence of a shaft pool had little effect on the residual energy (Fig. 4). But greater rate of energy dissipation was observed with the 90° outflow direction, all other parameters being identical. The finding is illustrated in Fig. 4 where the dimensionless residual head in Models B and D (90° outflow direction) are consistently smaller than those in Models A and C, especially in regimes R2 and R3. The result agrees with the study of Chanson (2002a) on the Valdepuentes dropshaft models.

Bubble swarm length

The dimensionless bubble penetration depth is plotted in Fig. 5 as a function of the dimensionless flow rate d_c/h for dropshaft configurations with deep pools, where D_{ab} is the visually-observed bubble plume length, y_p is the pool height above the outflow channel invert, and P is the pool depth (Fig. 2a). (In the absence of the shaft pool, bubble penetration was limited by the shaft invert.) In flow regimes R1 ($d_c/h < 0.04$) and R3 ($d_c/h > 0.05$), substantial flow aeration took place, the bubbles plunged deep down to the shaft pool and the bubble cloud occupied a sizeable shaft pool volume. In flow regime R2 ($0.04 \leq d_c/h \leq 0.05$), the nappe interacted with the downstream conduit inlet and lesser flow aeration was observed. In turn the bubble swarm was smaller.

Interestingly, visual observations of bubble penetration depth showed consistently smaller bubble swarm depths in the prototype (Fig. 5). The prototype observations were consistent with air concentration measurements conducted in the shaft pool (see air–water flow properties). It is likely that the result is related to

some form of scale effects as air entrainment cannot be scaled by a Froude similitude (Wood 1991; Chanson 1997).

Particle residence times

The residence times of neutrally-buoyant particles were measured in the shaft, where the residence time T was defined from take-off at the brink of the inflow channel to the entry into the outflow channel. Such particles were used to simulate the water flow behaviour and to characterize large-scale vortical structures. The results indicated that the residence time T was basically independent of the particle sizes (3.3 to 9 mm for the model and 5 to 15 mm for the prototype) for all flow regimes and configurations. For one dropshaft configuration and one flow regime, the probability distribution functions of dimensionless residence time $T V_c/d_c$ were nearly independent of the flow rate, where d_c is the critical depth at the inflow channel brink and V_c is the corresponding critical velocity. Hence, the data were regrouped for one geometry and one flow regime and a statistical summary is presented in Table 3.

Typical probability distribution functions of dimensionless residence times are presented in Fig. 6 for a dropshaft configuration with deep pool and 180° outflow direction. In regime R1, the dimensionless particle residence time was comparatively the greatest, corresponding to the entrainment of particles in the shaft pool and, sometimes, their trapping in large-size vortical structures for a significant duration. In the regime R2, the free-falling nappe flowed directly into the outflow channel. Most particles were directly entrained into the outflow conduit, corresponding to a very small residence time. The residence time was about the free-jet trajectory time. In the regime R3, particles were sometimes entrained down the shaft pool but most exited the shaft rapidly. The same trends were observed in both model and prototype, as emphasised by mean particle residence time results (Table 3).

Table 3. Distributions of dimensionless particle residence times TV_c/d_c — statistical summary.

| Configuration | Regime | No. of particles | TV_c/d_c | | | | | | | | | $(\text{Vol})(V_c)/Qd_c$, shaft pool |
			Mean	Std	Skew	Kurt	Min.	Max.	1st mode	2nd mode	
Prototype AA (180°)	R1	380	830	1150	1.87	3.22	13	5787	33	1230	769
	R2	86	188	503	3.56	13.3	5	2728	6	—	228
	R3	227	209	459	2.72	7.17	6	2543	14	750	127
Model A (180°)	R1	253	1050	1635	2.66	8.08	15	9580	66	1771	765
	R2	99	80	170	3.66	14.86	5	986	10	—	229
	R3	180	246	519	4.76	32.34	6	4706	18	490	124
Model B (90°)	R1	189	653	1119	3.06	12.02	27	7282	79	1272	829
	R3	292	111	117	5.46	46.62	14	1349	79	311	129
Model C (180°)	R1	59	51	55	2.25	6.26	2	289	7.5	—	43.8
	R3	60	53	60	2.01	3.53	11	274	12.5	—	17.4
Model D (90°)	R1	60	203	360	4.37	22.54	1	2327	32.5	—	55.5
	R3	65	31	14	1.34	2.16	12	78	27.5	—	17.1

Notes: Kurt, Fisher kurtosis; Skew, Fisher skewness; Vol, shaft pool volume; Q, flow rate.

Fig. 6. Probability distribution functions of dimensionless residence time TV_c/d_c. (a) Model A (180° outflow). (b) Prototype P2 (180° outflow).
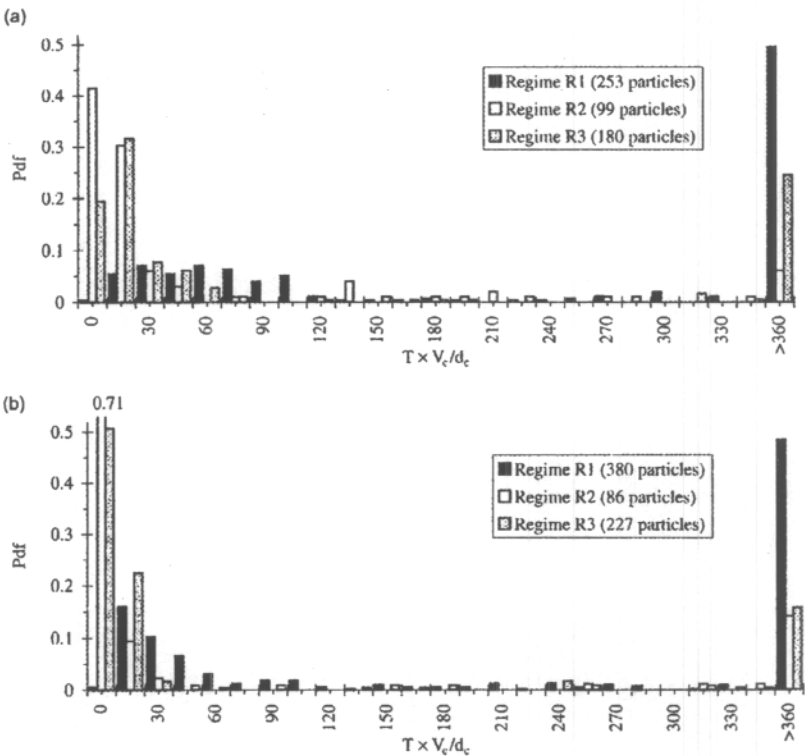
In regime R1, the residence time probability distributions exhibited a bi-modal shape. For the data shown in Fig. 6, Mode 1 is centered around $TV_c/d_c = 66$ and 33 for Model A and Prototype AA, respectively, while Mode 2 is centered roughly around $TV_c/d_c = 1770$ and 1230 for Model A and Prototype AA (Table 3). These values may be compared with the average filling time of the shaft pool of about $(\text{Vol}/Q)(V_c/d_c) = 770$, where Vol is the shaft pool volume (Table 3). Physically, about 40–

50% of the particles flowed downwards at nappe impact and were entrained rapidly into the outflow channel (Mode 1). The rest of the particles (i.e., 50–60%) were trapped in large-scale vortices (Mode 2). They were seen to recirculate in large-scale flow structures, sometimes passing from one structure to another, until they were finally entrained in the downstream conduit. In average, these Mode 2 particles stayed in the shaft pool for about 2.5 times the average filling time of shaft pool. In

regime R3, dimensionless particle residence time data also suggested a kind of bimodal distribution, although not as marked as in regime R1. The results are summarized in Table 3.

In a dropshaft with 90° outflow direction and deep pool, particles had to be subjected to a change in flow direction before exiting. Visually most particles tended to be entrained deep down the pool shaft, to twist around near the shaft bottom and to flow outwards rapidly. The same pattern was observed in both regimes R1 and R3. In turn, the mean residence times were smaller than those with the 180° shaft configuration (Table 3).

In dropshafts with 180° outflow direction, some particles were trapped for several minutes in large-scale vortical structures. Sometimes, particles were trapped in corner recirculation zones, below the outflow channel invert, before being entrained into the outflow conduit. These observations were noted on both model and prototype.

For dropshaft configurations without pool (models C and D), most particles exited rapidly. The mean residence time was typically 4 to 8 times shorter than those in deep pool shafts.

Discussion

A similar trend was noted between Model A and Prototype AA. However, prototype results suggested consistently smaller dimensionless residence times for all flow regimes (Fig. 6). Model data tended to overestimate residence times, and hence overestimated mass transfer rates, based upon a Froude similitude. Such observations imply some scale effect between model and prototype. It is believed that particle residence times is strongly related to vortical motion in the shaft pool, which cannot be scaled by a Froude similitude. (Vortical motion is dominated by viscous effects implying the need for Reynolds similitude.)

For all configurations, significant data scatter was noted, as evidenced by the large standard deviations of the dimensionless particle residence times (Table 3) and by the large maximum observed residence times (Table 3). The finding was surprising especially for the Models C and D (no pool).

Application to air–water mass transfer

Air–water flow properties

The experimental results demonstrated that both bubble swarm lengths and particle residence times were the greatest in the dropshaft configuration with deep pool and 180° outflow direction (Model A). In turn, this design (i.e., "Roman dropshaft") has the greatest potential for air–water transfer according to eq. [2].

Detailed air–water flow measurements were conducted with a sturdy single-tip conductivity probe in Prototype AA (Fig. 1, Table 4). Preliminary measurements conducted at various transverse locations y indicated that the void fraction distributions were basically two-dimensional, but next to the outside edges of the free-falling nappe impact. Measurements were conducted next to the jet centreline to characterize the two-dimensional

flow region while additional profiles were measured next to the jet outer edges (Table 4).

Typical distributions of void fraction C and dimensionless specific interface area ad_c are presented in Fig. 7, where x is the horizontal distance measured from the downstream shaft wall, z is the vertical direction positive downwards with $z = 0$ at the pool free-surface, and y is the horizontal transverse distance from the shaft centreline (Fig. 2). Experimental results in the Prototype AA demonstrated high void fractions next to the free-surface for all three discharges: that is, for $z \leq 50$ mm (Fig. 7). Large measured void fractions could not be attributed to measurement error: the plunge point region was visually aerated and it had an appearance somehow similar to a hydraulic jump roller. Furthermore, the pool free-surface elevation fluctuated at low frequency with time. (The natural sloshing period of the shaft pool was about 0.5 s.) It is conceivable that the probe tip was in air for brief periods, although this was not visually observed. Void fraction distributions showed that the measurements were performed in the fully-developed flow region: i.e., $10 \leq z/d_i \leq 70$ typically where d_i is the jet thickness at impact. For comparison, the experiments of Cummings and Chanson (1997) were conducted in the developing flow region corresponding to $z/d_i < 10$.

Distributions of specific interface areas exhibited a marked peak (Fig. 7) corresponding to a maximum of up to 140 m^{-1}. Such values are lower than observations in plunging jet flows with comparable impingement velocities (Cummings and Chanson 1997; Brattberg and Chanson 1998) (e.g., Fig. 3), but the present study was conducted with a coarser probe sensor than these studies (0.35 mm versus 0.025 mm). In the bubbly flow region, the cross-sectional averaged specific interface area a_{mean} ranged from 2 to 11.5 m^{-1} (Table 4) where

$$[5] \qquad a_{mean} = \frac{1}{BL} \int\limits_{y=-B/2}^{+B/2} \int\limits_{x=0}^{+L} a \, dx \, dy$$

in which B is the shaft width, L is the shaft length, and x and y are the horizontal coordinates (Fig. 2). In the shaft pool, the cumulative air–water interface area A ranged from 1.1 to 2.8 m^2 (Table 4) where

$$[6] \qquad A = \int\limits_{z=0}^{y_p+P} \int\limits_{y=-B/2}^{+B/2} \int\limits_{x=0}^{+L} a \, dx \, dy \, dz$$

Note that A is the cumulative interfacial area in the bubble swarm. It does not account for the shaft pool free-surface area BL.

Air–water mass transfer

If the bubble residence time and specific interface area are known, the mass transfer equation may be integrated along the

Table 4. Summary of air–water interfacial area measurements in dropshaft Prototype AA.

Q (m³/s)	Flow regime	V_i^* (m/s)	d_i^* (m)	$y_p^\dagger$ (m)	y (m)	z (m)	a_{mean} (1/m)	$A^\ddagger$ (m²)	Remarks
0	R1	5.81	0	0.02	0, 0.20, 0.22			1.12	$d_c = 0.02867$ m
						0.03	3.64		
						0.05	4.18		
						0.08	8.64		
						0.11	11.5		
						0.15	5.54		
						0.2	5.3		
						0.434	0		$z = D_{ab}$
0.02	R1	5.74	0	0.08	0, 0.20, 0.25			1.5	$d_c = 0.0471$ m
						0.03	10.7		
						0.08	11.6		
						0.15	6.52		
						0.25	4.46		
						0.35	1.97		
						0.416	0		$z = D_{ab}$
0.07	R3	5.58	N/A	0.266	0, 0.20, 0.30			2.84	$d_c = 0.12237$ m
						0.03	7.36		
						0.05	6.58		
						0.08	6.23		
						0.15	6.66		
						0.25	6.33		
						0.35	7.53		
						0.761	0		$z = D_{ab}$

*V_i and d_i, jet impact velocity and thickness deduced from trajectory equations.

†Measured.

‡Bubbly flow interface area only.

dropshaft. The results are often expressed in terms of the aeration efficiency E defined as

[7] $$E = \frac{(C_{gas})_{d/s} - (C_{gas})_{u/s}}{C_s - (C_{gas})_{u/s}}$$

where the subscript *u/s* and *d/s* refer to the upstream and downstream flow conditions. Assuming that the bubble residence time is about the same as the particle residence time, the integration of eq. [2] yields in first approximation

[8] $$E \approx 1 - \exp\left(-K_L \frac{A}{Vol} T\right)$$

where Vol is the shaft pool volume and T is the particle residence time. For the investigations in the Prototype AA, results are plotted in Fig. 8 in terms of oxygen transfer at 20 °C. They are compared with the empirical correlations of Avery and Novak (1978) and Nakasone (1987) developed for free-overfall and drop structures, and the correlation of Rahme et al. (1997) for circular dropshafts without a pool and 180° outflow direction.

Present results suggested a decrease in aeration rate with increasing flow rate. The trend is consistent with the findings of Avery and Novak (1978) and Rahme et al. (1997), although these studies used different configurations. Aeration rate was maximum at low flows (regime R1) because of larger residence time and significant aeration. Indeed similar interfacial properties were observed in both flow regimes R1 and R3 (Table 4), but the dimensionless residence times were on average four times larger in regime R1 (Table 3).

Discussion

The aeration efficiency results were one order of magnitude lower than the dissolved oxygen (DO) measurements and correlations. It is hypothesized that the underestimate derives from the instrumentation that could not detect bubble sizes smaller than 0.5 mm. With a 0.025 mm sensor, Cummings and Chanson (1997) measured interface area up to 1000 m⁻¹ (Fig. 3): that is, about one order of magnitude greater than present results. (For specific interface areas 10 times greater, the integration of eq. [2] would yield $E = 0.46$ to 0.21 for $Q = 0.0076$ to 0.067 m³/s.) Further, for a given probe sensor, eq. [4] underestimates the air–water interface area by 20% on average.

Summary and conclusions

Four configurations of rectangular dropshafts were investigated systematically to study the effects of outflow direction and pool depth on particle residence times and flow aeration. Shaft configurations without a pool were characterized by residence

Fig. 7. Dimensionless distributions of void fractions C and specific interface area ad_c. (a) Regime R1, $Q = 0.0076$ m³/s, $z = 0.050$, 0.110, 0.150 m. (b) Regime R3, $Q = 0.067$ m³/s, $z = 0.050$, 0.150, 0.250 m.

(a)

(b)
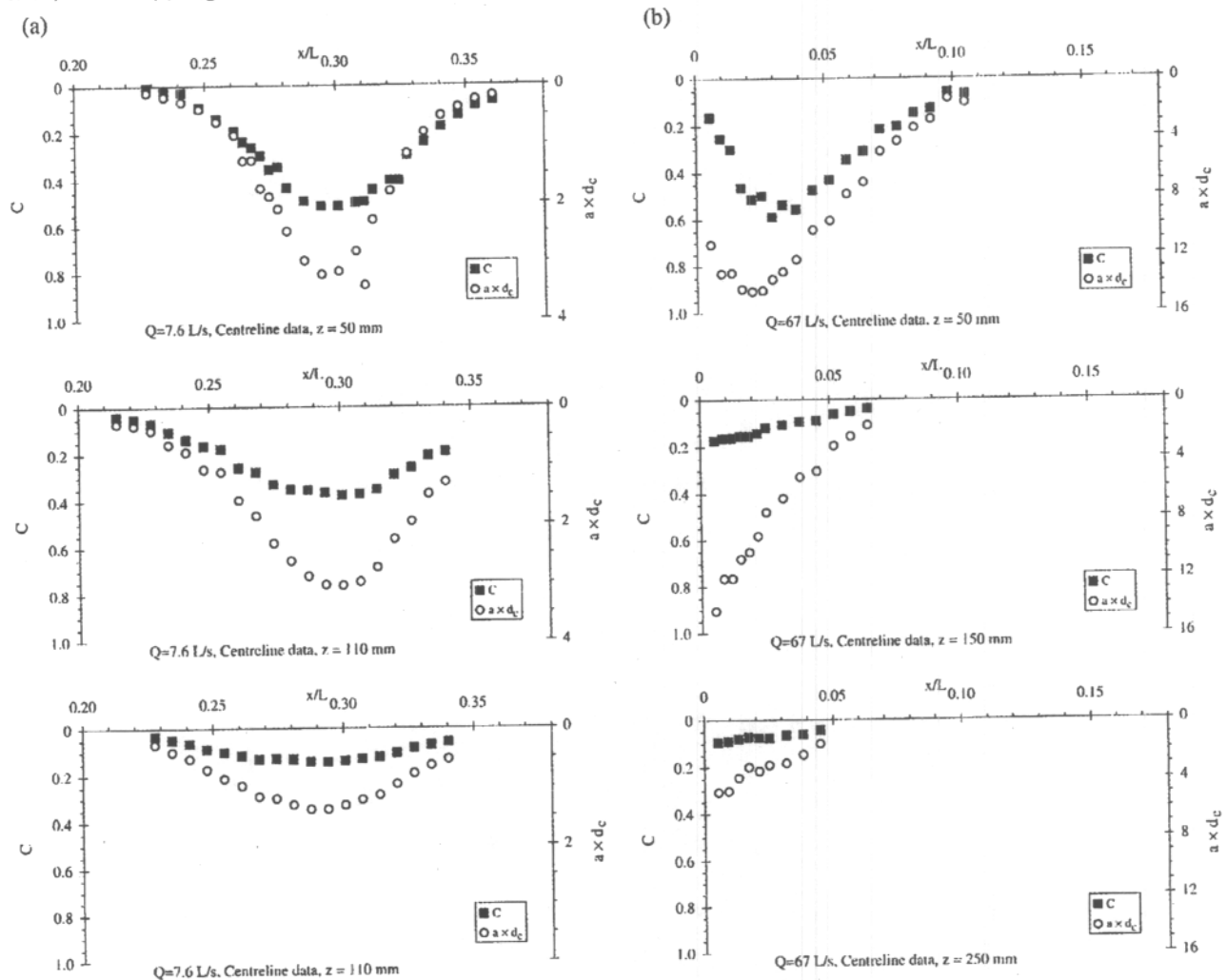
times 4 to 8 times shorter than those with deep pool shafts. The best design was that with 180° outflow direction and deep pool shaft (Model A), for which optimum operation was achieved at low flow rates (regime R1).

For the best design (Model A, "Roman dropshaft"), a full-scale study was conducted, the scaling ratio between proto-type and model being 3.1:1. Although similar trends were seen in both model and prototype, scale effects were observed in terms of particle residence times and bubble swarm depths. That is, model results overestimated dimensionless residence time TV_c/d_c and bubble penetration depth $D_{ab}/(y_p + P)$.

In the prototype, detailed air–water flow measurements were performed in the shaft pool. Distributions of void fractions and specific interface area exhibited maxima next to the impinge-ment point. The mass transfer equation was integrated using measured interfacial areas and particle residence times. The re-

sults demonstrate that the air–water mass transfer is the largest at low flow rates (regime R1) because of large residence times and significant interfacial area. Quantitative estimates of aera-tion efficiency in terms of dissolved oxygen appear lower than laboratory and prototype measurements at drop structures. It is suggested that the sturdy probe used in the present study could not detect fine bubbles and underestimated the interfacial area by one order of magnitude.

Overall the present study provides new understanding of the basic mechanisms of air–water mass transfer in rectangular dropshafts. Dropshaft performances are directly related to the residence times and flow aeration. The former is enhanced by deep shaft pools, especially at low flows, while the latter is significant for all flow rates (except for regime R2).

Interestingly the full-scale dropshaft was a 1:1 scale model of a dropshaft built by the Romans along the Yzeron aque-

Fig. 8. Aeration efficiency in terms of dissolved oxygen at 20 °C — comparison between the integration of the mass transfer equation (i.e., eq. [8]) and empirical correlations.
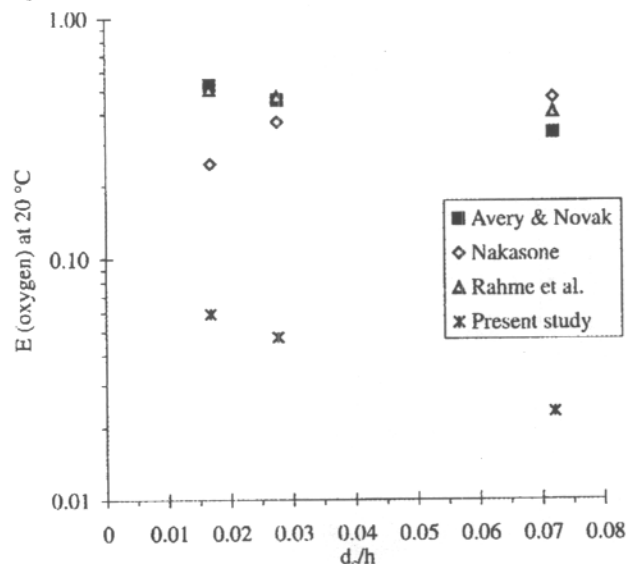
duct to supply water to the city of Lyon (France). That aqueduct was equipped with at least two series of at least two to six dropshafts each (possibly more). The design permitted to achieve DO saturation and to improve water quality. Definitely the Roman engineers produced an excellent design in terms of energy dissipation and flow aeration, particularly at low flow rates (regime R1).

Acknowledgments

References

Apelt, C.J. 1984. Goonyella Railway duplication drop structures and energy dissipators at culvert outlets. Model Studies. Report CH27/84, Department of Civil Engineering, University of Queensland, Australia. 10 p.

Avery, S.T., and Novak, P. 1978. Oxygen transfer at hydraulic structures. J. Hydraul. Div. Am. Soc. Civ. Eng. **104**(HY11): 1521–1540.

Brattberg, T., and Chanson, H. 1998. Air entrapment and air bubble dispersion at two-dimensional plunging water jets. Chem. Eng. Sci. **53**(24): 4113–4127. Errata: **54**(12): 1925.

Chanson, H. 1997. Air bubble entrainment in free-surface turbulent shear flows. Academic Press, London, UK.

Chanson, H. 1999. The hydraulics of open channel flows: An introduction. Edward Arnold, London, UK.

Chanson, H. 2002a. An experimental study of roman dropshaft hydraulics. J. Hydraul. Res. IAHR, **40**(1): 3–12.

Chanson, H,. 2002b. An experimental study of roman dropshaft operation: Hydraulics, two-phase flow, acoustics. Report CH50/02, Department of Civil Engineering, University of Queensland, Brisbane, Australia. 99 p.

Chanson, H. 2004. The hydraulics of open channel flows: An introduction. 2nd ed. Butterworth-Heinemann, London, UK.

Clark, N.N., and Turtom, R. 1988. Chord length distributions related to bubble size distributions in multiphase flows. Int. J. Multiphase Flow, **14**(4): 413–424.

Corsi, R.L., Shepherd, J., Kalich, L., Monteith, H., and Melcer, H. (1992). Oxygen transfer and VOC emissions from sewer drop structures. In Proceedings of 1992 National Conference on Hydraulic Engineering, Water Forum '92, Baltimore, Md., 3–5 August 1992. Edited by M.E. Jennings and N.G. Bhowmik. ASCE, New York, USA. pp. 305–310.

Cummings, P.D., and Chanson, H. 1997. Air entrainment in the developing flow region of plunging jets. Part 2: Experimental. J. Fluids Eng. **119**(3): 603–608.

Gulliver, J.S. 1990. Introduction to air–water mass transfer. In Proceedings of the 2nd International Symposium on Gas Transfer at Water Surfaces, Air-Water Mass Transfer, Minneapolis, Minn., 9–14 September 1990. Edited by S.C. Wilhelms and J.S. Gulliver. ASCE, pp. 1–7.

Henderson, F.M. 1966. Open channel flow. MacMillan Company, New York.

Jirka, G.H. 1991. Gas transfer processes at the air/water interface. In Environmental Hydraulics. Edited by J.H.E. Lee and Y.K. Cheung. Balkema, Rotterdam, The Netherlands. pp. 357–370.

Kawase, Y., and Moo-Young, M. 1992. Correlations for liquid-phase mass transfer coefficients in bubble column reactors with Newtonian and non-Newtonian fluids. Can. J. Chem. Eng. **70**: 48–54.

Merlein, J., Kleinschroth, A., and Valentin, F. 2002. Systematisierung von Absturzbauwerken. Mitterilung No. 69, Lehrstuhls fur Hydraulik und Gewasserkunde, Technishen Universitat Munchen, Germany, 206 p.

Moursali, E., Marié, J.L., and Bataille, J. 1995. An upward turbulent bubbly boundary layer along a vertical flat plate. Int. J. Multiphase Flow, **21**(1): 107–117.

Nakasone, H. 1987. Study of aeration at weirs and cascades. J. Environ. Eng. ASCE, **113**(1): 64–81.

Rahme, Z.G., Zytner, R.G., Corsi, R.L., and Madani-Isfahani, M. 1997. Predicting oxygen uptake and VOC emissions at enclosed drop structures. J. Environ. Eng. (Reston, Va.), **123**(1): 47–53.

Rajaratnam, N., Mainali, A., and Hsung, C.Y. 1997. Observations on flow in vertical dropshafts in urban drainage systems. J. Environ. Eng. ASCE, **123**(5): 486–491.

Sene, K.J. 1984. Aspects of bubbly two-phase flow. Ph.D. thesis, Trinity College, Cambridge, UK.

Toda, K., and Inoue, K. 1999. Hydraulic design of intake structures of deeply located underground tunnel systems. Water Sci. Technol. **39**(9): 137–144.

Vischer, D., and Hager, W.H. 1998. Dam hydraulics. John Wiley, Chichester, UK. 316 p.

Wood, I.R. 1991. Air entrainment in free-surface flows. IAHR Hydraulic Structures Design Manual No. 4, Hydraulic Design Considerations, Balkema, Rotterdam, The Netherlands. 149 p.

List of symbols

A gas–liquid interface area (m²) in the shaft pool

a specific interface area (m⁻¹) defined as the air–water surface area per unit volume of air and water

a_{mean} mean interface area (m⁻¹) in a horizontal cross-section

B dropshaft width (m)

b open channel width (m)

C air concentration defined as the volume of air per unit volume of air and water; it is also called void fraction

C_{gas} concentration of dissolved gas in water (kg/m³)

D 1-conduit diameter (m) and 2-conduit height (m)

D_{ab} bubble penetration depth (m) measured vertically from the free-surface

D_{gas} molecular diffusivity of gas in water (m²/s)

d flow depth (m) measured perpendicular to the channel bed

d_c critical flow depth (m); in a rectangular channel: $d_c = \sqrt[3]{q^2/g}$

d_i nappe thickness (m) at impact: i.e., thickness of the free-falling jet at impact

E aeration efficiency

F air bubble count rate (Hz) defined as the number of detected air bubbles divided by the scanning time;

g gravity constant (m/s²); $g = 9.80$ m/s² in Brisbane

H total head (m)

H_{res} residual head (m): $H_{res} = H_1 - \Delta H$

H_1 upstream total head (m)

h drop (m) in invert elevation

K_L liquid film coefficient (m/s)

L dropshaft length (m)

L_R geometric scaling ratio: i.e., ratio of prototype to model dimensions

l brink overhanging (m) over the shaft

M_{gas} mass of dissolved gas (kg)

P (shaft) pool height (m), measured from the shaft bottom to the downstream conduit invert

Q total volume discharge (m³/s) of water

q discharge per meter width (m²/s); for a rectangular channel: $q = Q/b$

T particle residence time (s) in the shaft

t time (s)

V velocity (m/s)

V_c critical flow velocity (m/s); for a rectangular channel: $V_c = \sqrt{gd_c}$

V_i velocity (m/s) at nappe impact

Vol   shaft pool volume (m³): Vol $= (P + y_p)BL$

x horizontal Cartesian co-ordinate (m) measured from the downstream shaft wall

y transverse distance (m) measured from the shaft centreline

Y_p free-surface height (m) in a shaft pool above the downstream conduit invert

z vertical distance (m) the pool free-surface, positive downwards

ΔH head loss (m): i.e., change in total head

$\varnothing$ diameter (m)

Subscripts

c critical flow conditions

i nappe impact flow conditions

1   upstream or inflow conditions

2   downstream or outflow conditions